




## Article

# Flame-Front Rate of Spread Estimates for Moderate Scale Experimental Fires Are Strongly Influenced by Measurement Approach

Joshua M. Johnston <sup>1,2,\*</sup> , Melanie J. Wheatley <sup>1,3</sup>, Martin J. Wooster <sup>2,4</sup> , Ronan Paugam <sup>2,5</sup> , G. Matt Davies <sup>6</sup> and Kaitlin A. DeBoer <sup>1</sup>

<sup>1</sup> Canadian Forest Service, Great Lakes Forestry Centre, 1219 Queen Street E, Sault Ste Marie, ON P6A 2E5, Canada; Melanie.Wheatley@ontario.ca (M.J.W.); kaitlin.deboer@canada.ca (K.A.D.)

<sup>2</sup> King's College London, Department of Geography, Strand, London WC2R 2LS, UK; martin.wooster@kcl.ac.uk (M.J.W.); ronan.paugam@gmail.com (R.P.)

<sup>3</sup> Aviation Forest Fire and Emergency Services, Ontario Ministry of Natural Resources and Forestry, 95 Ghost Lake Road, Dryden, ON P8N 0A2, Canada

<sup>4</sup> Natural Environment Research Council (NERC) National Centre for Earth Observation (NCEO) at King's College London, Strand, London WC2R 2LS, UK

<sup>5</sup> College of Forest Resources, University of Washington, Mailbox 352100, Seattle, WA 98195, USA

<sup>6</sup> School of Environment and Natural Resources, The Ohio State University, Kottman Hall, 2021 Coffey Road, Columbus, OH 43210, USA; davies.411@osu.edu

\* Correspondence: joshua.johnston@canada.ca

Received: 15 April 2018; Accepted: 4 May 2018; Published: 9 May 2018



**Abstract:** Understanding wildfire rate of spread (RoS) is often a key objective of many fire behavior modelling and measurement exercises. Using instrumented moderate scale laboratory burns we provide an assessment of eight different methods of flame front RoS determination, including visible imagery (VIS) analysis techniques, use of thermocouple arrays, and four thermal infrared (IR) image analysis approaches. We are able to (1) determine how measurement approach influences derived RoS, and (2) recommend the best method to reproduce the accepted standard (Thermocouple Grid Array measurement) RoS without ground sampling. We find that derived RoS is statistically significantly influenced by the measurement approach, and that failing to fully account for directionality of the RoS may result in significant error. We identify one of the thermal infrared imaging methods (described in Paugam et al. 2013), as the most appropriate for providing rate and direction of spread at these scales of measurement.

**Keywords:** wildfire rate of spread; fire behavior; fire intensity; Thermocouple; infrared imaging; method selection; visible imagery

## 1. Introduction

Wildfire behavior can be described as the manner in which a spreading fire reacts to changes in its environment with respect to fuels, topography, and weather. Changes in wildfire behavior have substantial impacts on the safety of fire suppression operations and the tactics that must be employed [1]. The primary indicators of fire behavior are rate of spread (RoS) and Byram's fire intensity (FI; [2–4]). Wildfire RoS is the rate of forward advancement of the flame front in a spreading fire. RoS determination is an important area of wildfire research [5–8], and often the primary objective of many fire measurement and behavior modelling exercises [9–11]. The importance of RoS extends to its operational use, as it is crucial for assessing the safety of ground crews responding to wildfire [1,12–15]. The current and expected RoS of a fire can determine the utility of escape routes and contribute to

predicting the probability of fire entrapment [16]. RoS is also vital in calculating Byram's fire intensity (here after referred to as "fire intensity"), which has been considered the single most valuable metric for describing a wildfire [2,4]. Fire intensity corresponds to the success of suppression strategies [17]; fires with high intensity ( $>4000 \text{ kW m}^{-1}$ ) often cannot be contained by initial attack and result in increased area burned and suppression costs. Knowledge of both fire intensity and RoS allow researchers to make further inferences about the behavior and ecological effects of fires, such as their fuel consumption, depth of burn, seed viability, and vegetation mortality [18–21].

Fire intensity is calculated in terms of the available fuel energy released in the flame front and RoS as in Equation 1, where FI is the fireline intensity ( $\text{kW m}^{-1}$ ),  $H$  is the low heat of combustion ( $\text{kJ kg}^{-1}$ ),  $W$  is the weight of the fuel consumed ( $\text{kg m}^{-2}$ ), and  $R$  is RoS ( $\text{m s}^{-1}$ ), [3]. RoS is by far the most temporally variable of the parameters that contribute to fire intensity because it is controlled, in part, by wind speed (e.g., [22]); while fuel consumption and heat of combustion [23] are related to fuel structure, chemistry, and moisture [10].

$$FI = H \times W \times R \quad (1)$$

Accurate measurement of RoS is challenging (due to limitations in site access and confounding factors such as smoke obscuration, temporal instability in RoS and direction of travel, radiative preheating of instruments, and more), and there are consequences for inaccurate representations of this parameter [24]. For example, in operational applications of the Canadian Forest Fire Behavior Prediction System (CFFBPS) [10], fire intensity is often subdivided into discrete intensity classes (IC), which are used extensively in the field guide for the CFFBPS [25]. A minor deviation in RoS has the potential to alter the intensity class, making accurate measurement of RoS essential.

A summary of select RoS measurement methods is provided in Table 1. Standard methods for measuring RoS, include visual observations—essentially surveying fire arrival times at specific locations [26–28]. Visual methods of RoS estimation using visible-wavelength cameras are common in the laboratory where fire arrival time is observed and documented at fixed locations (with the camera view arranged linearly perpendicular to the direction of travel) throughout the fuel bed [29–32]. Visual observations are often the only RoS method available on wildfires using landscape features and observations from an aircraft [27]. Limitations of visual observations of RoS estimation include obscuration due to flame tilt, smoke masking, and perspective view (when the camera is operated from the ground). Butler et al. (2016) evaluated video observation of RoS against other methods (arrival times estimated with IR imagery and time lag between fire arrival at ground sensor positions), and found it to be the least reliable [32]. More recently, the use of thermocouples and data loggers has become increasingly popular and they can provide time series of temperatures at the fuel bed level [33]. Thermocouples determine fire arrival times by means of temperature thresholds (e.g.,  $\sim 573 \text{ K}$  for flaming combustion) [34]. The conventional (on-ground) means of documenting RoS is based on establishing a systematic grid sampling system over the experimental plot ( $\sim 10\text{--}20\text{m}$  spacing) and documenting fire arrival times at each point on the grid [35]. RoS is then computed using a series of equations [26,28], which calculates RoS as the distance travelled over three points in a triangle and the arrival time at each vertex, allowing RoS to be computed in the direction of spread. Although this method is considered the accepted standard for measuring RoS (e.g., [34,36–39]), it requires pre-burn site access, which makes its implementation on wildfires nearly impossible. The increasing availability of infrared (IR) imagers has led to the development of further remote sensing techniques for measuring RoS, beyond those using visible cameras (e.g., [8,35]). IR RoS methods are fundamentally similar to the use of thermocouples to determine fire arrival times using temperature time series, however, the ability to image these temperature series enables IR methods to directly observe the morphology of the perimeter and direction of spread (e.g., [8]). IR imaging allows RoS to be assessed much more readily on wildfires, since ground access and pre-burn set-up is not necessary. Studies have shown that IR imaging can provide more detailed spatial and temporal information on RoS compared to conventional thermocouple and visual methods of data capture [8,35].

Although some studies have considered coincident RoS observations of experimental fires [32], to date there has been no focused effort to compare RoS estimation techniques statistically. In this study, we assess multiple methods for RoS assessment. Few studies have attempted to assess and compare methods of RoS determination because of the complexity of studying large-scale fires. However, moderate-scale experimental burning ( $4.8 \times 7.3$  m) presents an opportunity to conduct laboratory quality experiments while allowing fires to accelerate to a steady state, creating ideal conditions for such a comparative study. We have two objectives (1) determine how measurement approach influences derived RoS, and (2) recommend the best method to reproduce the accepted standard (thermocouple grid array measurement), RoS without ground sampling. Overall, we use eight different approaches to derive RoS data on 27 moderate-scale experimental fires, spanning visual imagery, thermocouple arrays, and IR imaging.

## 2. Methodology

### 2.1. Experimental Design and Protocol

Twenty seven moderate-scale ( $4.8 \times 7.3$  m) experimental fires were burned during 2013 and 2014 to support this study. Burns were conducted at the Canadian Forest Service's Rose Experimental Burn Station, an open-air facility 11 km northwest of Thessalon, Ontario, Canada. Thermal imaging cameras were mounted on a 30 m scaffold tower above a constructed burn platform. Experimental fires were sampled on the basis of three rows of four ( $1.21 \times 2.43$  m) panels (see Figure 1) using fuel beds constructed out of dried longleaf pine (*Pinus palustris*) needles. Details on fuel bed construction and fuel characterization are described elsewhere [40] including additional monitoring of fire intensity. Two different IR cameras, the Agema 550 and the FLIR SC6703, described in detail in [40], were used in 2013 and 2014, respectively. Visible cameras were paired with the IR cameras, and additional visible imagery was collected from the side viewing position (Figure 2).

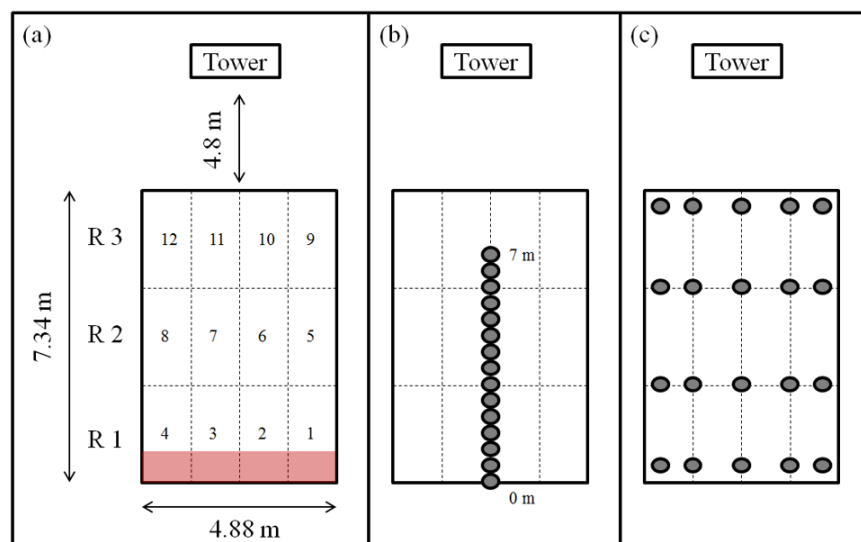


**Figure 1.** Burn platform layout and naming conventions and the two primary patterns for fuel bed thermocouples (TC). The platform layout (a) was organized with each panel numbered (1–12) and each row of panels labelled (1–3), the red region along the edge or R1 represents the ignition zone. TC layouts were given two primary configurations; the linear array (b) was predominantly used in the 2013 campaign, while the gridded array (c) was used in 2014. For the linear array, thermocouples were spaced at 0.5 m intervals beginning at the plot edge (0 m) and terminating 7 m into the pad. In the gridded arrangement, thermocouples were placed at the junction points of each panel. Along the edges of the pad these sensors were moved inward by 0.3 cm to ensure contact with flame fronts.

A standard forestry drip torch containing a mixture of 3:1, diesel to gasoline fuels, was used to ignite the fuel beds. An ignition line involving all fuels was laid up to approximately 0.5 m into the fuel bed for all burns (Figure 1a). This was achieved by beginning at one end of the west side of the platform and placing a series of tightly-spaced ignition lines perpendicular to the edge of the fuel bed while walking towards the opposing side. This ignition pattern assisted the fire in accelerating to an equilibrium combustion state as rapidly as possible, which was important given the relatively short (max 8 m) distance available for spread. Minimizing or removing the “acceleration” stage of fire growth was desirable.

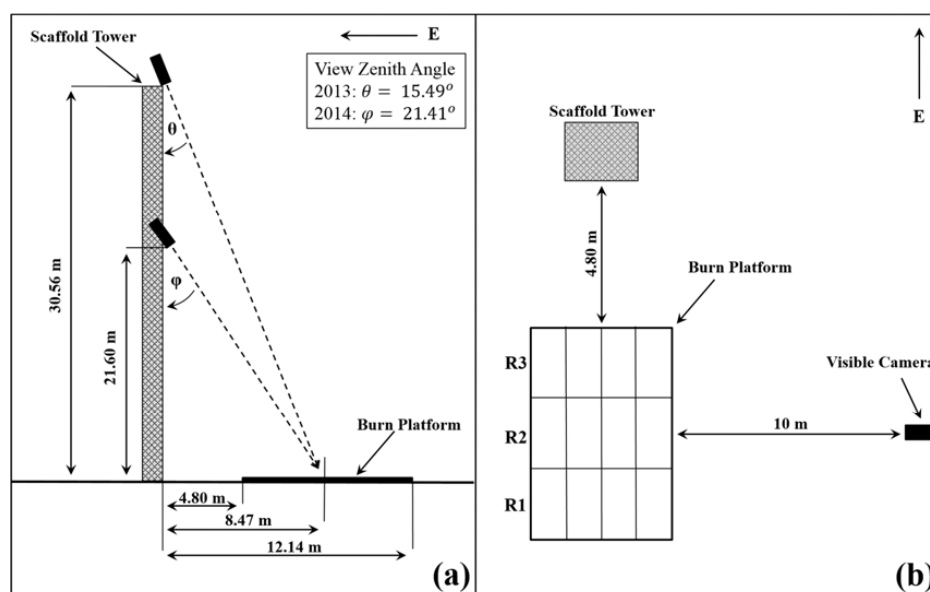


**Figure 2.** Positioning of the visible (VIS) and infrared (IR) cameras relative to burn platform. (a) Placement of the IR and VIS cameras on the scaffold tower gave view zenith angles of 15.49 and 21.41° in 2013 and 2014 respectively. (b) In both 2013 and 2014 the side viewing VIS camera was placed 10 m south of the burn platform aligned with the center of row 2.

## 2.2. Methods of Calculating Rate of Spread

General descriptions of each of these methods, as well as the data collection, are described in Table 1 along with the naming conventions used to refer to these methods throughout the study. Not all of these methods were applied to all burns. Table S1 outlines which methods were applied to each burn.

### 2.2.1. Visible Side and Visible Nadir Methods

Visible imagery was analyzed from the ground level (side viewing) and the tower position (near nadir viewing) to determine fire arrival times. The visible-wavelength (VIS) camera at near nadir viewing was positioned alongside the mid-wave IR thermal imaging camera at the top of the tower (i.e., viewing the fuel bed from above), and the side viewing camera was positioned on the ground centered along the length of the platform (i.e., viewing the spreading fires from the side). RoS was determined by visually observing when the fire first crossed into each of the separate rows of the burn platform and recording the timestamp of the imagery at that point. The series of arrival times were then differenced to determine the time it took for the fire to cross each row (a distance of ~2.43 m), which allowed the calculation of its RoS ( $\text{m s}^{-1}$ ). In this case, a forward (east) spread direction is assumed (based on ignition pattern [40]), and RoS is only measured along the length of the burn platform. These methods simulate applications from airborne and ground level observations of flame front RoS [27,36,37], where time is reported for the travel of fire between two fixed points.

**Table 1.** Overview of the various Rate of Spread (RoS) calculation methods employed in this study.

Method Reference	Method Description	Data Source	Fire Arrival Threshold	Direction of Spread	Field Deployment	Data Processing	Number of Fires with Data Available
Visible Side	Fire spread recorded with VIS camera at ground level. Visual analysis to determine time lapse between fixed locations.	VIS Imagery	Visual	NA	Ground observations	Manual interpretation, minimal calculation	27
Visible Nadir	Fire spread recorded with VIS camera on tower at near nadir position. Visual analysis to determine time lapse between fixed locations.	VIS Imagery	Visual	NA	Aircraft observation	Manual interpretation, minimal calculation	27
Thermocouple Linear Array	Linear array of 15 thermocouples at 0.5 m intervals extending perpendicular to the ignition line along the center of the burn platform. Fire arrival determined at each position via temperature threshold.	Thermocouples	573 K	NA	Ground instrumentation	Partially automated, minimal calculation	27
Thermocouple Grid Array	Grid of 20 thermocouples positioned uniformly throughout the burn platform. Fire arrival determined at each position via temperature threshold. Arrival times used in Simard et al. (1984) method, averages for each panel of burn pad reported.	Thermocouples	573 K	Geometrically calculated	Ground instrumentation	Partially automated	7
Infrared Grid Array	Geo-referenced nadir positioned IR brightness temperature time series used to replace the 20 thermocouples in the thermocouple grid method, otherwise method remains unchanged.	IR Imagery	773 K	Geometrically calculated	Airborne IR (requires geo-referencing)	Fully automated, computationally intensive	24
Paugam et al. (2013)	Direct application of the method of Paugam et al. (2013). Bonfire ground control points are not used due to fixed IR camera position on top of nearby tower. Flame front arrival is determined via brightness temperature threshold and RoS computed normal to the flame at each pixel.	IR Imagery	650 K	Normal at each pixel	Airborne IR (requires geo-referencing)	Fully automated, computationally intensive	24
Paugam et al. (2013) 773 K	Variant of the IR Paugam et al. (2013) methodology in which the fire arrival temperature threshold is raised to 773 K.	IR Imagery	773 K	Normal at each pixel	Airborne IR (requires geo-referencing)	Fully automated, computationally intensive	24
Infrared Triangular Method	Variant of the method described in McRae et al. (2005). In this method IR imagery is geo-referenced, and calculations are performed directly on raster data. Fire arrival times from adjacent perimeter pixels are used in the Simard et al. (1984) method and reported by pixel.	IR Imagery	773 K	Geometrically calculated by pixel cluster	Airborne IR (requires geo-referencing)	Fully automated, computationally intensive	24

### 2.2.2. Thermocouple Linear Array

The thermocouple temperature time series was used to determine fire arrival times using IDL [41] computer code and a fixed temperature threshold of 573 K [34]. The use of 573 K (300 °C) as the temperature threshold for fire arrival thermocouples is a standard approach in fire research corresponding to flaming combustion and visible flame tip thresholds [34,42]. The fire arrival times were then used to determine the time required for the fire to travel between adjacent thermocouples to determine RoS. For the 2013 burns, a linear array was constructed of 15 K-type 24-gauge (0.56 mm) thermocouples spaced 0.5 m apart and extending down the central line of the burn platform. In 2014, the linear arrival times were determined by examining only the four thermocouples in the same central position of the gridded arrangement (see Figure 1b,c). Where certain thermocouples failed during burns, the arrival times of the next closest positions were compared to give the time lapsed over the new distance. The RoS values were averaged to produce a single value for each row. The data was logged at 2 Hz using a Campbell CR-1000 data logger for the full duration of each burn.

### 2.2.3. Thermocouple Grid Array (Standard Method)

Similar to the thermocouple linear array, a fixed temperature threshold of 573 K was used to determine fire arrival time. However, a grid configuration consisting of 20 thermocouples in the 2014 burns was used to improve the ability to measure non-directional rate of spread. This layout was not feasible during the 2013 measurements due to the large quantity of other equipment deployed on those fires. Fire arrival times were used in groups of three to compute rate and direction of spread using the triangular method [26] (see Figure S1). Each panel of the burn platform was framed by four points (Figure 1c), allowing for four different triangles to be used in the calculation for each panel. The average RoS and direction (DIR) of the four results were reported to describe each panel. These results were then averaged across each row. Since the rise in temperature for thermocouples is very steep, it allows the flame front arrival time to be calculated with great certainty. The data was logged at 2 Hz using a Campbell CR-1000 data logger for the full duration of each burn. This method is the accepted standard in RoS measurement, in this study this method is used to rate the performance of other techniques.

### 2.2.4. Infrared Grid Array

The IR grid method was identical to the thermocouple grid method except instead of thermocouples we used the pixel brightness temperature (BT) time series corresponding to thermocouple locations. Determining fire arrival time is different using IR imagery than thermocouples. Thermocouples record a rise in temperature at (or slightly after) the arrival of the flame front at their position on the surface of the fuel bed. Typically, in an advancing fire the flame body leans over the unburnt fuel bed and causes the temperature series at a fixed point to appear (from a nadir view point) to rise before the flame front actually reaches that point on the fuel bed surface (Figure 3). Some of the inconsistencies in brightness temperatures as compared to thermocouple temperatures are also related to flame emissivity and thermocouple placement, which are illustrated in Figure 3. When the flame front is spreading actively with wind influence the flame tips have the potential to cause the IR temperature to rise well in advance of the actual arrival of the flame front at the fuel bed level. When the fire is advancing against the wind direction or spreading under low wind conditions the influence of the flame tips is less pronounced. A visualization of the variability of this time lag can be seen in Figure 4. In this study these uncertainties are small, however under crown fire conditions it is possible for flame lengths to be an order of magnitude greater, resulting in larger uncertainty. Therefore, it is necessary to ensure that the IR fire arrival temperature is calibrated for the current spatial resolution to minimize this potential error. Conversely the thermocouple arrival time tends to be more consistent, presenting a spike in the temperature values with a similar time lag to fire arrival. Based on previous analysis [40], it was



determined that an infrared BT threshold of 773 K was optimal to achieve the most consistent fire arrival times under these experimental conditions.

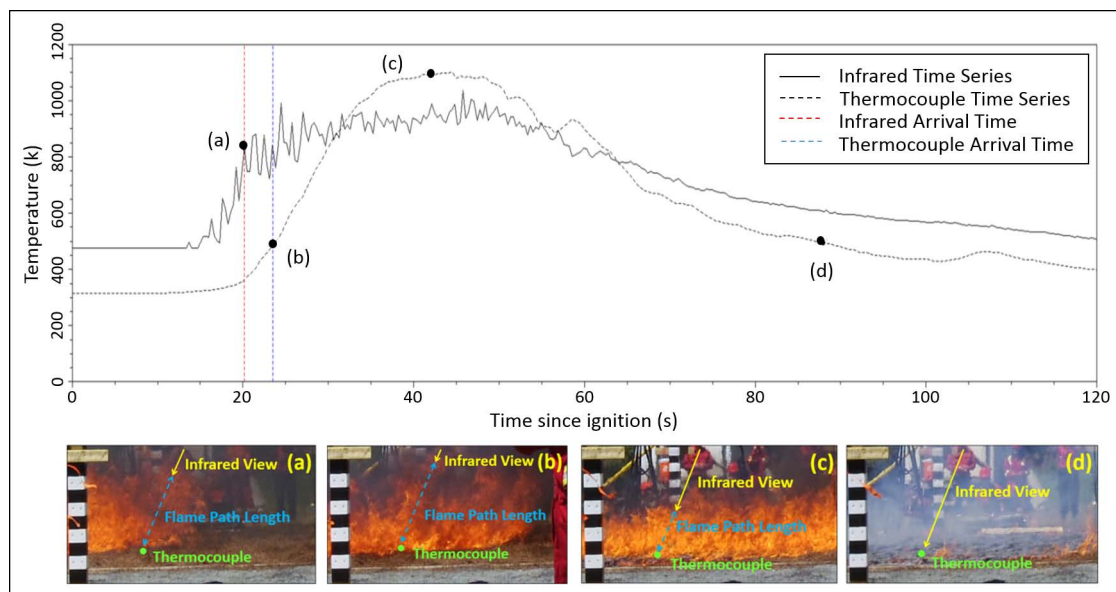


**Figure 3.** Thermocouple (dotted line) and Infrared (IR; solid line) temperature series for a single position 2.5 m from the western edge along center line of the burn pad during burn 1 on 12 June 2013, with descriptive side viewing imagery. The IR temperature series produced here is from the Agema 550 operating in the 573–973 K temperature range. Points a, b, c, and d along the time series correspond to the images presented beneath the plot where observation path of the IR camera are illustrated by the yellow arrow labelled “Infrared View”, the flame which intersects this observation path is illustrated in blue labelled “Flame Path Length” and the position of the thermocouple is presented in green. In ((a);  $T = 20.2$  s), the IR time series triggers an arrival (using the derived 773 K arrival threshold), it can be seen that though this threshold has been reached there is a time lag of  $\sim 3$  seconds before the thermocouple is triggered at the lower arrival threshold of 573 K ((b);  $T = 23.5$  s). During this phase of the burn, while the flames are observed clearly by the IR camera, the thermocouple is insulated from full exposure to the flame by unburnt fuel. The depth of the flame in the IR viewing path reaches its maximum of  $\sim 0.8$  m (and therefore its highest emissivity [43]), resulting in peak temperatures being observed in the IR time series. This is not the case as the flame reaches the thermocouple directly ((c);  $T = 42.0$  s). At this stage, peak temperatures, which exceed those in the IR, are observed in the thermocouple time series as the depth of the flame obscures the observation path ( $\sim 0.4$  m) and remains insufficient to achieve black body behavior (achieved at  $\sim 4$  m [43]). The relationship is then inverted again as smoldering combustion begins ((d);  $T = 88.0$  s). At this stage the IR temperatures rise above the thermocouple again as the thermocouple is now fully exposed above the smoldering fuels and subject to cooling by ambient wind flow.

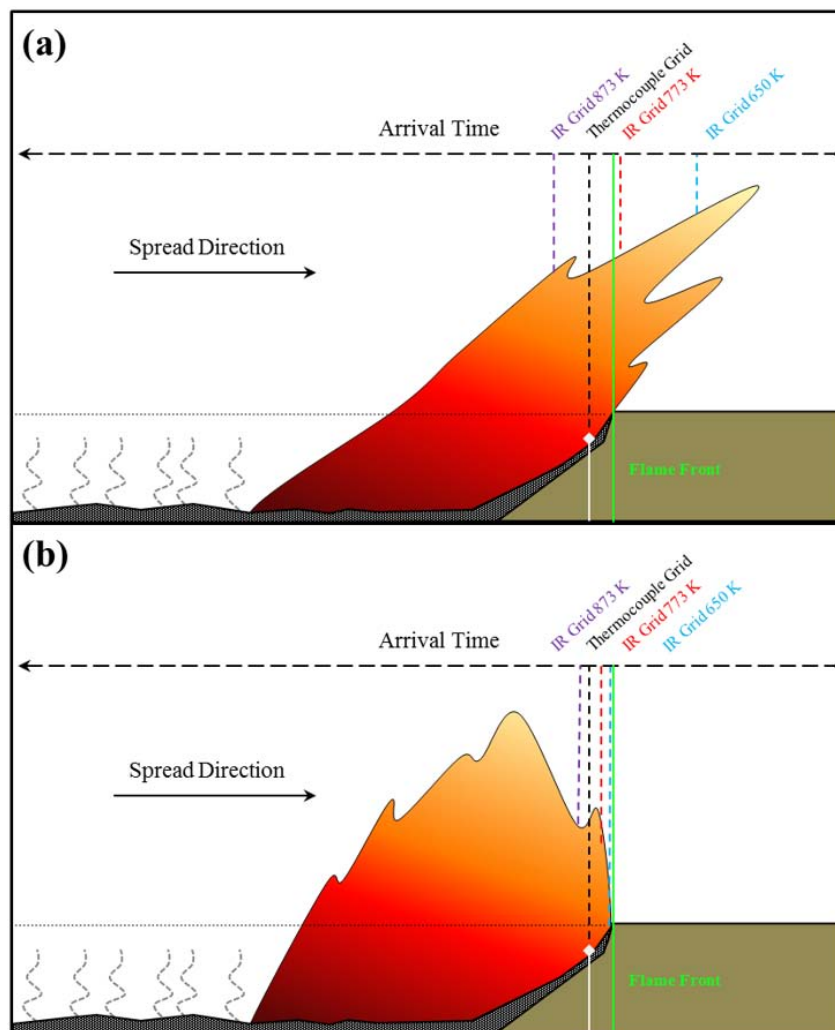


**Figure 4.** Visualization of the challenges associated with determining the flame front position at the fuel bed level, which is where combustion is initiated and the fire actually arrives at a location. Two scenarios are presented here, the flame front leaning over the unburned fuel (a) and the flame front positioned vertically (b). The arrival time lines are arranged to demonstrate the relative position in a time series of varying methods of determining the fires arrival time. Fluctuation between (a) and (b) conditions (due to changes in wind and topography), make IR arrival times difficult to predict. Here three IR arrival thresholds (650, 773, and 873 K) are depicted in a theoretical manner.

#### 2.2.5. Infrared Paugam et al. 2013 Based Methods

Paugam et al. (2013) identified flame fronts in infrared imagery using an IR BT threshold of 650 K, whereas our revised version used a threshold of 773 K (as in [40]). These thresholds are designed to locate all pixels in an IR image that are along the leading perimeter of the flame front (excluding those within the flame body and smoldering areas). Use of an elevated threshold is appropriate here given the very small pixel size (~1–3 cm, degraded to 13 cm during geo-referencing) that can be considered filled by flame, however at coarser spatial resolutions this may not be the case due to mixing of smoldering and flaming combustion at the sub-pixel level. In this study we examine method performance at both arrival thresholds to examine sensitivity to this parameter.

A time series of flame front perimeters was generated and used to determine the direction of spread at each pixel by examining the local normal to the fire perimeter at its location. The distance travelled along the normal between successive perimeters (a minimum of 2 successive images are required) in the time series was used to calculate the RoS at each pixel along the flame front. In this



way rate and direction of spread is produced for as many pixels as possible (excluding those that have normal vectors extending outside the burn platform) along the perimeter at each time step.

These methods produce a large number of RoS data points, not only for a burn, but also for each time step of the sampling. They also provide descriptions of the direction of spread at each point (refer to Figure 5 for an example of a single time step). With the large amount of RoS data produced by this method, characterizing a dataset to give a single representative value for each row for later comparison needed to be done with care. A detailed examination of the distribution of the RoS data was conducted at varying scales for a few exemplar burns (see Figure S2). At every level of sampling (e.g., whole experiment by individual points, whole experiment by row, individual burn, single sample step), calculated RoS is typically not normally distributed and there are often outlier points, which tend to be biased towards high RoS values. The median values of all data points were reported (as recommended by McRae et al., 2005 [35]) by row to resist outliers.

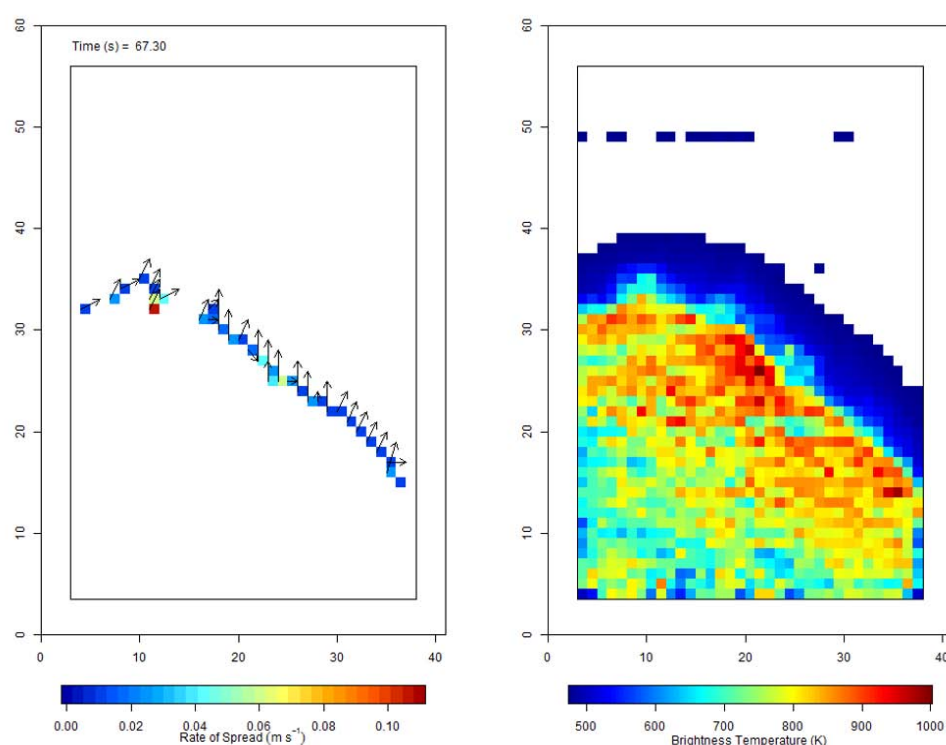


**Figure 5.** Rate and direction of spread calculated using the method of Paugam et al. (2013) for the 14 June 2013 burn. The results are presented for a single time step (67.30 s after ignition). Axes are given in pixels (0.13 m), the rectangular burn platform area is outlined in black within the plot area. On the right the brightness temperature (BT) map is presented for this time step, where no color is produced the temperature was below the calibration range of the AGEMA 550 at the current setting (i.e., below ~473 K). Notably a few pixels in a horizontal line can be seen rising above the threshold in front of the flame front, these are caused by IR radiation from the fire heating an overhead cable connected to other instrumentation not used in this study. These artifacts were masked out of analysis. The left image presents the corresponding RoS (pixel color) and direction of spread (arrows) for each flame front pixel identified in the BT map using the Paugam et al. (2013) method, vectors indicate direction of spread.

## 2.2.6. Infrared Triangular Method

This method is a variant of the method used by McRae et al. (2005) and relies on IR imagery to determine fire arrival times for each pixel in the burned area, and then computes RoS using the Simard et al. (1984) equations for successive pixels in triangular groupings. The original McRae et al.

(2005) method was deployed on fires that remained sub-canopy, resulting in a low fire arrival threshold (423 K) to allow for canopy interception of the IR signal and therefore lower pixel temperatures. These arrival values were then used to produce RoS for pixel groups using the Simard et al. (1984) equations and the results were interpolated to yield a complete map of RoS for the burn.

The infrared triangular method used in this study differs from McRae et al. (2005) for several reasons. First, the arrival threshold was raised to 773 K based on previous analysis [40] and due to the substantially different spatial resolution and observation conditions of this experiment. Second, no interpolation was applied; gaps in the data were not considered to be significant given the higher spatial resolution. In the present implementation the arrival threshold was used to produce a time series of the flame front arrival at pixel locations along each perimeter. Each flame front was segmented into discrete vertices with a spacing of roughly 0.5 m between them. The vertices of adjacent flame fronts were used to apply the Simard et al. (1984) equation to triangular subsets. The rate and direction of spread were reported at each point.

### 2.3. Analysis

For each method and burn, three RoS values were calculated by row. Although an effort was made to compute RoS with all methods for all burns, sensor failure, IR camera malfunction, and other issues occasionally prevented the use of all methods. For example, a search was performed on the data after the experiment to find thermocouples that failed during a burn. The entire time series for the failed sensor(s) was discarded for the burn in question, regardless of when it failed. This was done as a precaution since thermocouples can produce erroneous readings in the moments preceding sensor failure. However, RoS was often still calculable using the next nearest thermocouples. To help aid in the interpretation and validity of the thermocouple data, these series were compared to the time synchronized visible imagery.

To maximize the certainty of the results of the IR imagery, each frame of each burn was geo-referenced separately. Even though the camera was placed on a stationary tower, geo-referencing was still required because the camera was viewing at an angle and so burn platform pixels closer to the tower were smaller than those further away, and also sometimes the camera was moved slightly in the wind. The tower itself is 4.80 m to the east of the burn platform, and with the camera 30.56 m and 21.6 m up the tower in 2013 and 2014, respectively, the view zenith angles were 15.49 and 21.41 degrees to the center of the burn platform (Figure 2a). Paugam et al. (2013) demonstrated some of the advantages to geo-referencing data from IR imaging devices to ensure consistent spatial extents of each pixel when performing quantitative analyses. Geo-referencing and application of a direct linear transformation (DLT) converted the varying pixel sizes of the angled view to a uniform dimension for all pixels (as described in Paugam et al. (2013) [7] and Pastor et al. (2006) [38]).

A linear mixed effects model was used to determine if the selection of RoS method had a significant impact on the RoS estimated. This method was used to allow analysis at the row level while accounting for repeated observations on the same fire, as well as to focus on differences in method performance while accounting for differences in behavior fires. The method of RoS measurement was treated as a fixed effect in the model. The effects of Burn and Row and the interaction between Burn and Row were considered as random effects in the model. A linear regression analysis with a test of the deviation from the ideal Line of Perfect Agreement (LPA) was used to determine which measurement of RoS produced the best agreement with the Thermocouple Grid Array method. The R programming language was used for all statistical analysis [44]. The linear mixed modelling analysis was conducted using the lme4 (e.g., the “lmer” function) [45] and lmerTest (e.g., the “anova” and “summary” functions) [46] R packages were used to provide p values for the mixed modelling analysis.

### 3. Results

The distribution of RoS measurements for each method is presented in Figure 6a, for each burn in Figure 6b, and for each row (over all burns) in Figure 6c. Notably, row 1 displays significantly higher RoS values than rows 2 and 3 as result of the ignition pattern (see Figure 6c).

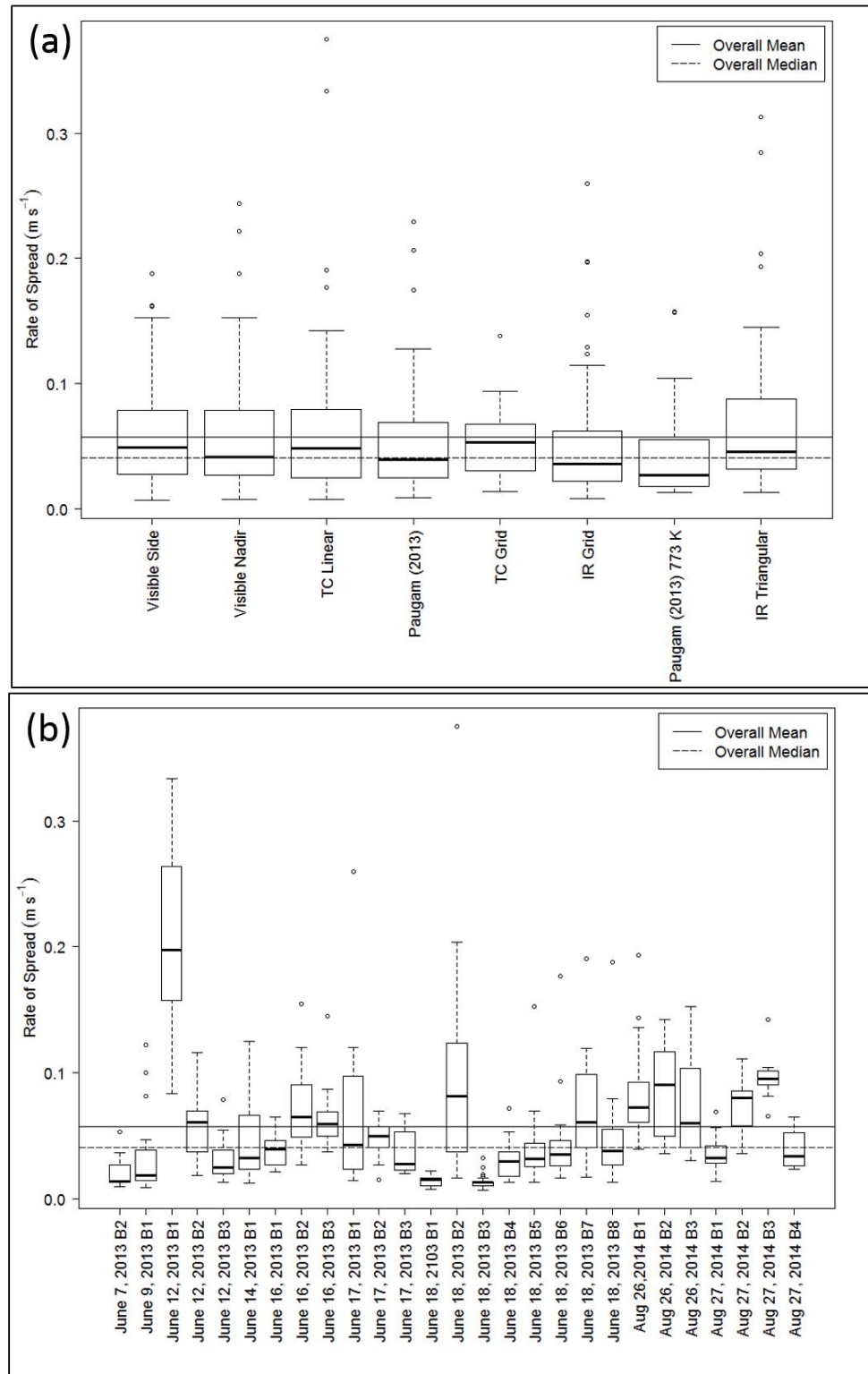
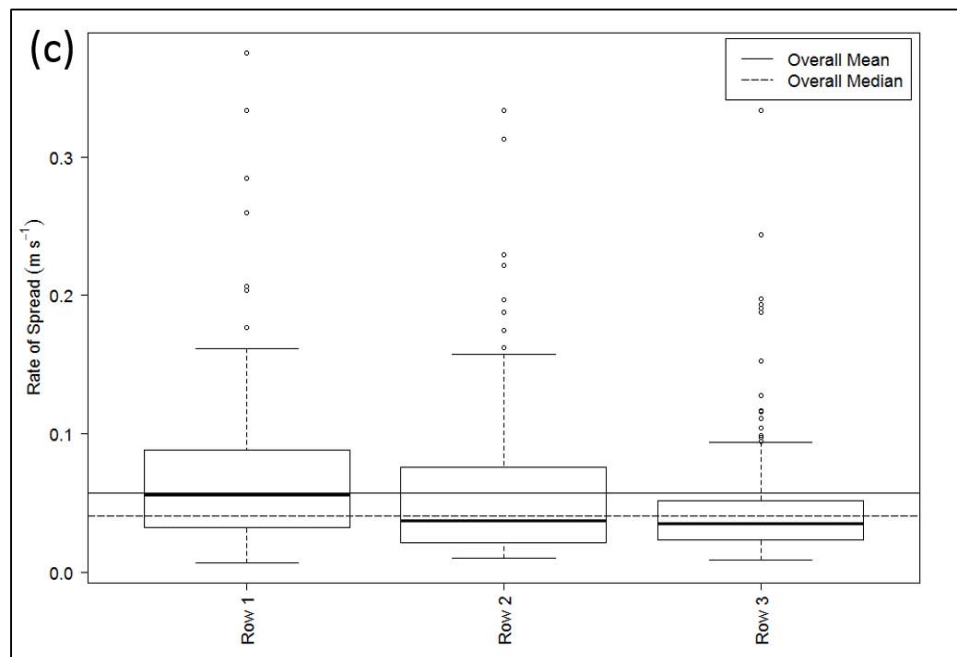


Figure 6. Cont.



**Figure 6.** Rate of spread (RoS) boxplots for 2013-2014 experimental burns grouped by (a) RoS assessment method, (b) burn identifier, and (c) row of burn platform. For (b), burns are identified by date and “ $B_i$ ” to indicate burn number (e.g.,  $i = 1, 2, 3, \dots$ ). (c) Boxplot of all rate of spread (RoS) measurements made for each burn of the 2013 and 2014 experimental burn data, presented by row of the burn platform. The mean and median RoS values for all methods combined are plotted as horizontal lines over all methods.

### 3.1. Comparison of Methods to One Another

In the linear mixed effects model, the random effects were initially allowed to vary in terms of both intercept and slope for each method. However, restricting the random effects to vary only by intercept significantly improved the model, as seen in substantial reductions in both Akaike Information Criterion (AIC;  $\Delta_{AIC} = -33.4$ ) and in Bayesian Information Criterion (BIC;  $\Delta_{BIC} = -329.5$ ). The simplified model was then tested against a further reduction in complexity that excluded the random Burn  $\times$  Row interaction. Using the likelihood ratio test, it was found that including this interaction significantly affected the model ( $\chi^2(1) = 5.77$ ,  $p < 0.000$ ,  $\alpha = 0.05$ ). Additionally, removal of this interaction resulted in a large increase in AIC ( $\Delta_{AIC} = +43.6$ ) and in BIC ( $\Delta_{BIC} = +39.3$ ) suggesting that its inclusion benefits the model. Tables S2 and S3 present a complete description of the final model.

**Table 2.** Significance of the deviation of RoS methods from the accepted standard (Thermocouple Grid Array) RoS.  $T$ -test’s use the Satterthwaite’s approximation for degrees of freedom (DF).

Fixed Effect (RoS Method)	DF	$T$	$p$
Visible side	425.2	1.176	0.240
Visible nadir	425.2	1.340	0.181
Thermocouple Linear Array	426.1	2.591	0.010 *
Infrared Grid Array	427.1	1.211	0.227
Paugam et al. (2013)	427.0	0.749	0.454
Paugam et al. (2013) 773 K	426.9	−0.500	0.618
Infrared Triangular Method	426.9	2.352	0.019 *

\* Significance values of  $p$  based on  $\alpha = 0.05$ .

The linear mixed modelling results were analyzed using lmerTest package [46] and showed that the method of measurement had a significant impact on observed RoS ( $p < 0.000$ ). Not all methods showed agreement with the Thermocouple Grid Array approach of RoS (Table 2). Significant deviations were observed for the Linear Thermocouple Array method ( $p = 0.010$ ), and the Infrared Triangular ( $p = 0.019$ ) method.

### 3.2. Comparison of Measurements to Accepted Standard

To determine which method produced the best agreement with the Thermocouple Grid Array approach, the remaining three IR methods (Infrared Grid Array, Paugam et al. (2013) and Paugam et al. (2013) 773 K) were compared directly to the standard method using a linear regression analysis and comparison to the ideal LPA (as in [35,47]). All three regressions produced significant relationships with the Thermocouple Grid Array (see Figure 7), with the Paugam et al. (2013) 773 K showing the best relationship ( $R^2 = 0.77$ ,  $p < 0.000$ ), while the agreement in the Infrared Grid Array method is comparable ( $R^2 = 0.75$ ,  $p < 0.000$ ), followed by the Paugam et al. (2013) method ( $R^2 = 0.42$ ,  $p < 0.032$ ). In addition, the regressions showed no significant deviation in slope from the LPA whilst the LPA remained within the 95% CI of the regression (see Table 3).

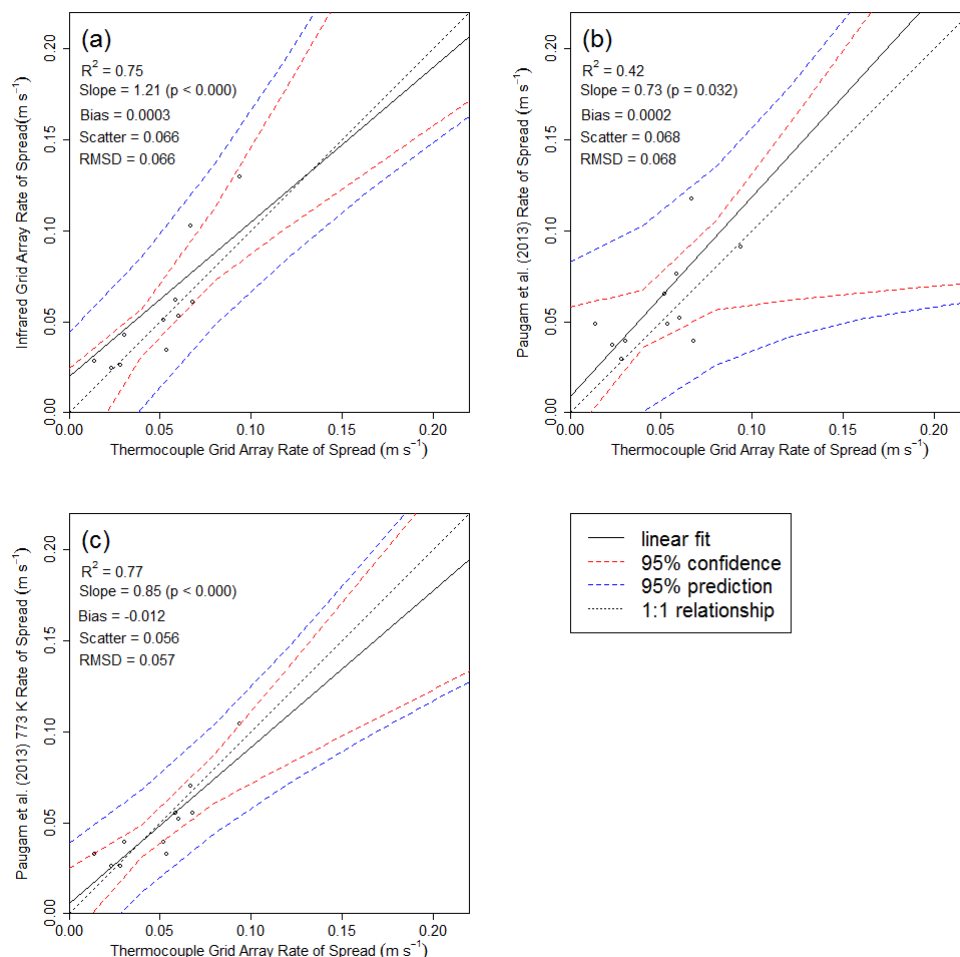


**Figure 7.** Linear regression results comparing mean thermocouple grid rate of spread (RoS) values to the (a) Infrared Grid Array (b) Paugam et al. (2013) and (c) Paugam et al. (2013) 773 K methods RoS values for each row of the 2014 experimental burns.

**Table 3.** Testing the deviation from the line of perfect agreement of regressions ( $\alpha = 0.05$ ).

RoS Method	DF	Critical $T$	Slope	SE	$T$	$p$
Infrared Grid Array	8	2.306	1.123	0.234	−0.526	0.613
Paugam et al. (2013)	8	2.306	0.733	0.289	0.924	0.383
Paugam et al. (2013) 773 K	8	2.306	0.858	0.158	0.899	0.395

#### 4. Discussion and Conclusions

This study suggests that the method used to determine RoS has a significant impact on the derived values at the type of moderate-scale experimental fires used herein. Given that different methods of measurement have the potential to alter the observed RoS, they also have the potential to affect the estimated fire intensity and corresponding reported fire behavior. This is significant as in operational settings, fire intensity is divided into intensity classes used to guide management responses [25,28]. As can be seen in Table 4, although there are clear distinctions in the qualitative fire behavior observed, under fixed fuel consumption and low heat of combustion (H) values, the range of RoS from one intensity class (IC), to the next is small. For example, assuming an H of  $\sim 18,000 \text{ kJ kg}^{-1}$  and a fuel consumption of  $0.9 \text{ kg m}^{-2}$ , IC 2 has a RoS range of only  $0.033 \text{ m s}^{-1}$  ( $< 2 \text{ m min}^{-1}$ ), and IC 3 has a range of just  $0.96 \text{ m s}^{-1}$  ( $5.77 \text{ m min}^{-1}$ ), with the ranges progressively increasing as the IC increases. With a required accuracy of  $\pm 0.033 \text{ m s}^{-1}$  differences in IC could easily be attributed to method choice and result in substantially different estimated fire behavior. In this study 63% of the burns were assigned conflicting IC values due to disagreement in RoS methods. This misrepresentation in IC could result in operational response differences, including resource allocation of fire crews, equipment (hand tools vs pump and hose), and air attack, contributing to excess costs or ineffective suppression.

**Table 4.** The Canadian Forest Fire Behavior Prediction System (CFFBPS) field guide intensity classes (IC) for describing fire behavior based on fire intensity ranges [26] with adjoining physical descriptions of the fire.

Intensity Class	Fire Intensity ( $\text{kW m}^{-1}$ )	Rate of Spread ( $\text{m s}^{-1}$ )	Description
1	<10	<0.001	Smoldering/creeping
2	10–500	0.001–0.032	Surface fire with open flame, flame heights $\sim 1.0 \text{ m}$
3	500–2000	0.033–0.12	Vigorous surface fire with short-range spotting
4	2000–4000	0.12–0.25	Intermittent crown fire
5	4000–10,000	0.25–0.64	Continuous crown fire, major suppression campaign
6	>10,000	>0.64	Continuous crown fire with extreme fire behavior, limited suppression potential

Of the methods not requiring ground sampling, the Paugam et al. (2013) 773 K method was the best representation of the Thermocouple Grid Array results. The Infrared Grid Array also had a strong relationship with the Thermocouple Grid Array, indicating that an increased BT threshold appears to improve the ability of these methods to describe the actual movement of the flame front at the fuel bed level and therefore RoS. The Thermocouple Linear Array and Infrared Triangular methods failed to produce valid RoS observations as compared to the standard.

The ability of the raised BT threshold to improve results is likely due to the smaller pixel size over the published applications and associated higher peak pixel temperatures (as flames tend to fill the entire pixel area at the present scale). For different pixel sizes, this threshold would need to be revised—and this could be done by resampling the radiances recorded by the current imagery to the new pixel size to be investigated. For applications using actual airborne and wildfire data it is recommended that perimeters are identified using the standard tactical mapping methods (e.g., [48,49]) for the detector system and edge detection of these pixel clusters.



Considering that the method of RoS assessment has an impact on the values of RoS derived, to characterize a highly variable parameter accurately it is important to: (1) ensure that observations are made of the correct value (e.g., flame front position at the fuel bed level and in the correct direction of spread) and, (2) collect as many observations as possible without sacrificing accuracy. It is evident that the Paugam et al. (2013) method, with a locally calibrated arrival threshold temperature, meets these criteria for observing RoS and is recommended for implementation where IR imagery of spreading fires is available. As an added advantage this is one of the few methods examined that can be deployed at scales ranging from moderate-sized experimental burns up to wildfires. That said, where possible the inclusion of ground-based thermocouples can substantially improve the fire arrival time thresholds.

The results of this study provide implications for operational wildfire practices. Although it may be necessary to characterize RoS to the utmost accuracy and capture its full variability along a flame front for research activities, this level of detail is not necessarily required for operational management purposes. This study suggests that RoS measurement using most methods is acceptable in describing the progression of a flame front, however, the failure of the Linear Thermocouple Array method suggests that failing to account for directionality in RoS measurement may result in significant error. For this reason, where visual observations are required for operational sampling of wildfire RoS, inclusion of the directional component is strongly encouraged (e.g., [26]). Notably, these results were generated under extremely controlled conditions (in terms of fuels homogeneity, slope, and sensor deployment), allowing the influence of RoS method to be detected in the analysis. It is possible that under less controlled conditions (e.g., large scale experimental burns or wildfires), the impact of RoS method may be less obvious, although still present.

In this study, eight methods of measuring RoS consisting of visual imagery, thermocouples, and IR imagery were evaluated. This study has shown that the method of measuring RoS has a significant impact on the RoS observed. In particular, the Paugam et al. (2013) 773 K method was the most effective at reproducing the accepted standard in RoS measurement. Notably, the 773 K threshold is tailored to the current experimental conditions and may not be ideal elsewhere. The Infrared Grid Array also had a strong relationship with the accepted standard.

**Supplementary Materials:** The following are available online at <http://www.mdpi.com/2571-6255/1/1/16/s1>, Table S1: Rate of spread (RoS) sampling methods for each burn conducted during the moderate-scale experimental campaigns; Table S2: Linear mixed modelling results summary for random effects; Table S3: Linear mixed modelling results summary for fixed effects; Figure S1: Distribution of the values needed to compute direction and rate of spread based on fire arrival time at three points forming a triangle according to the method of Simard et al. (1984); Figure S2: Normalized frequency distributions of rate of spread (RoS) values produced using the Paugam et al. (2013) 773 K method presented at varying sample scales.

**Author Contributions:** Johnston, Wooster and Paugam conceived and designed the experiments, and performed them with others acknowledged. Johnston analyzed the data; Davies contributed to statistical analysis; Wheatley, Johnston and DeBoer wrote the paper.

**Acknowledgments:** The authors thank John Studens, Alison Newbery, Alan Cantin, Dan Thompson, Natasha Jurko, Bruce Main, Francois Gonard, Mike Wotton, Jon Atherton, and Ralph Beeby for their assistance in the execution of the experimental burns. We also thank Rachel her insightful comments on the early manuscript. We would also like to thank the reviewers of this manuscript for their insightful and constructive suggestions. Critical support for this project was provided by the Canadian Space Agency and the European Space Agency. Martin Wooster's work is supported by the UK Natural Environmental Research Council (NERC) and NERC grant NE/J014060/1 supported some of the work described herein.

**Conflicts of Interest:** The authors declare no conflict of interest.

## References

1. Butler, B.; Cohen, J. Firefighter safety zones: A theoretical model based on radiative heating. *Int. J. Wildland Fire* **1998**, *8*, 73–77. [[CrossRef](#)]
2. Alexander, M.E. Calculating and interpreting forest fire intensities. *Can. J. Bot.* **1982**, *60*, 349–357. [[CrossRef](#)]
3. Byram, G.M. Forest fire behavior. In *Forest Fire: Control and Use*; Davis, K.P., Ed.; McGraw-Hill: New York, NY, USA, 1959; pp. 90–123.

4. Van Wagner, C.E. Describing forest fires—Old ways and new. *For. Chron.* **1965**, *41*, 301–305. [[CrossRef](#)]
5. Johnston, P.; Kelso, J.; Milne, G.J. Efficient simulation of wildfire spread on an irregular grid. *Int. J. Wildland Fire* **2008**, *17*, 614–627. [[CrossRef](#)]
6. Cruz, M.G. Monte carlo-based ensemble method for prediction of grassland fire spread. *Int. J. Wildland Fire* **2010**, *19*, 521–530. [[CrossRef](#)]
7. Andrews, P.L.; Cruz, M.G.; Rothermel, R.C. Examination of the wind speed limit function in the rothermel surface fire spread model. *Int. J. Wildland Fire* **2013**, *22*, 959–969. [[CrossRef](#)]
8. Paugam, R.; Wooster, M.J.; Roberts, G. Use of handheld thermal imager data for airborne mapping of fire radiative power and energy and flame front rate of spread. *IEEE Trans. Geosci. Remote Sens.* **2013**, *51*, 1–15. [[CrossRef](#)]
9. McArthur, A.G. *Fire Behaviour in Eucalypt Forests*; Forestry and Timber Bureau: Canberra, Australia, 1967.
10. Forestry Canada Fire Danger Group. *Development and Structure of the Canadian Forest Fire Behavior Prediction System*; Information Report St-X-3; Forestry Canada, Ed.; Forestry Canada, Science and Sustainable Development Directorate: Ottawa, ON, Canada, 1992.
11. Rothermel, R.C. *A Mathematical Model for Predicting Fire Spread in Wildland Fuels*; Res. Pap. Int-115; Department of Agriculture, Intermountain Forest and Range Experiment Station: Ogden, UT, USA, 1972; p. 40.
12. Butler, B.W. Wildland firefighter safety zones: A review of past science and summary of future needs. *Int. J. Wildland Fire* **2014**, *23*, 295–308. [[CrossRef](#)]
13. Putnam, T.; Butler, B.W. Evaluating fire shelter performance in experimental crown fires. *Can. J. For. Res.* **2004**, *34*, 1600–1615. [[CrossRef](#)]
14. Sullivan, A.L.; Knight, I.K.; Cheney, N.P. Predicting the radiant heat flux from burning logs in a forest following a fire. *Aust. For.* **2002**, *65*, 59–67. [[CrossRef](#)]
15. Zárate, L.; Arnaldos, J.; Casal, J. Establishing safety distances for wildland fires. *Fire Saf. J.* **2008**, *43*, 565–575. [[CrossRef](#)]
16. Fryer, G.K.; Dennison, P.E.; Cova, T.J. Wildland firefighter entrapment avoidance: Modelling evacuation triggers. *Int. J. Wildland Fire* **2013**, *22*, 883–893. [[CrossRef](#)]
17. Alexander, M.E.; Cole, F.V. *Predicting and Interpreting Fire Intensities in Alaskan Black Spruce Forests Using the Canadian System of Fire Danger Rating*; Society of American Foresters/Canadian Institute of Forestry Convention 1994, Bethesda, Maryland, 1995; Society of American Foresters: Bethesda, MA, USA, 1994; pp. 185–192.
18. De Groot, W.J. Modeling fire effects: Integrating fire behavior and fire ecology. In Proceedings of the 6th International Conference on Forest Fire Research, Coimbra, Portugal, 15–18 November 2010.
19. De Groot, W.J.; Bothwell, P.M.; Taylor, S.W.; Wotton, B.M.; Stocks, B.J.; Alexander, M.E. Jack pine regeneration and crown fires. *Can. J. For. Res.* **2004**, *34*, 1634–1641. [[CrossRef](#)]
20. De Groot, W.J.; McRae, D.J.; Ivanova, G.A. Modeling fire behaviour, fuel consumption and wildlandfire carbon emissions in Canadian and Russian boreal forests. In Proceedings of the 3rd International Fire Ecology and Management Congress, San Diego, TX, USA, 13–17 November 2006.
21. Smith, A.M.S.; Talhelm, A.F.; Johnson, D.M.; Sparks, A.M.; Kolden, C.A.; Yedinak, K.M.; Apostol, K.G.; Tinkham, W.T.; Abatzoglou, J.T.; Lutz, J.A.; et al. Effects of fire radiative energy density dose on pinus contorta and larix occidentalis seedling physiology and mortality. *Int. J. Wildland Fire* **2017**, *26*, 82–94. [[CrossRef](#)]
22. Albini, F.A. A model for fire spread in wildland fuels by-radiation. *Combust. Sci. Technol.* **1985**, *42*, 229–258. [[CrossRef](#)]
23. Rivera, J.d.D.; Davies, G.M.; Jahn, W. Flammability and the heat of combustion of natural fuels: A review. *Combust. Sci. Technol.* **2012**, *184*, 224–242. [[CrossRef](#)]
24. Simard, A.J.; Deacon, A.G.; Adams, K.B. Nondirectional sampling of wildland fire spread. *Fire Technol.* **1982**, *18*, 221–228. [[CrossRef](#)]
25. Taylor, S.W.; Pike, R.G.; Alexander, M.E. *Field Guide to the Canadian Forest Fire Behaviour Prediction (fbp) System*; Canadian Forest Service, Ed.; Northern Forestry Centre: Edmonton, AB, Canada, 1997.
26. Simard, A.J.; Eenigenburg, J.E.; Adams, K.B.; Nissen, J.R.L.; Deacon, A.G. A general procedure for sampling and analyzing wildland fire spread. *For. Sci.* **1984**, *30*, 51–64.
27. Alexander, M.E.; Lanoville, R.A. Wildfires as a source of fire behavior data: A case study from Northwest Territories, Canada. In Proceedings of the Ninth Conference on Fire and Forest Meteorology, San Diego, CA, USA, 21–24 April 1987.

28. Alexander, M.E.; Lawson, B.D.; Stocks, B.J.; van Wagner, C.E. *User Guide to the Canadian Forest Fire Behaviour Prediction System: Rate of Spread Relationships*; (Interim Edition); Environment Canada, Canadian Forestry Service: Northern Forest Research Centre: Edmonton, AB, Canada, 1984.
29. Wotton, B.; Martin, T. Temperature Variation in Vertical Flames from a Surface Fire. In *Proceedings of the III International Conference on Forest Fire Research/14th Conference on Forest and Fire Meteorology*, Luso, Portugal, 16–20 November 1998; pp. 533–545.
30. Mendes-Lopes, J.; Ventura, J.; Amaral, J. Flame characteristics, temperature-time curves, and rate of spread in fires propagating in a bed of pinus pinaster needles. *Int. J. Wildland Fire* **2003**, *12*, 67–84. [[CrossRef](#)]
31. Dupuy, J.; Maréchal, J.; Portier, D.; Valette, J.-C. The effects of slope and fuel bed width on laboratory fire behaviour. *Int. J. Wildland Fire* **2011**, *20*, 272–288. [[CrossRef](#)]
32. Butler, B.; Teske, C.; Jimenez, D.; O'Brien, J.; Sopko, P.; Wold, C.; Vosburgh, M.; Hornsby, B.; Loudermilk, E. Observations of energy transport and rate of spreads from low-intensity fires in longleaf pine habitat—RxCADRE 2012. *Int. J. Wildland Fire* **2016**, *25*, 76–89. [[CrossRef](#)]
33. Taylor, S.W.; Wotton, B.M.; Alexander, M.E.; Dalrymple, G.N. Variation in wind and crown fire behaviour in a northern jack pine-black spruce forest. *Can. J. For. Res.* **2004**, *34*, 1561–1576. [[CrossRef](#)]
34. Wotton, B.; Gould, J.; McCaw, W.; Cheney, N.; Taylor, S. Flame temperature and residence time of fires in dry eucalypt forest. *Int. J. Wildland Fire* **2012**, *21*, 270–281. [[CrossRef](#)]
35. McRae, D.J.; Jin, J.Z.; Conard, S.G.; Sukhinin, A.I.; Ivanova, G.A.; Blake, T.W. Infrared characterization of fine-scale variability in behavior of boreal forest fires. *Can. J. For. Res.* **2005**, *35*, 2194–2206. [[CrossRef](#)]
36. Stocks, B.J. Fire behaviour in immature jack pine. *Can. J. For. Res.* **1987**, *17*, 80–86. [[CrossRef](#)]
37. Stocks, B.J. Fire behaviour in mature jack pine. *Can. J. For. Res.* **1989**, *19*, 783–790. [[CrossRef](#)]
38. Pastor, E.; Àgueda, A.; Andrade-Cetto, J.; Muñoz, M.; Pérez, Y.; Planas, E. Computing the rate of spread of linear flame fronts by thermal image processing. *Fire Saf. J.* **2006**, *41*, 569–579. [[CrossRef](#)]
39. Stephens, S.L.; Weise, D.R.; Fry, D.L.; Keiffer, R.J.; Dawson, J.; Koo, E.; Potts, J.B.; Pagni, P.J. Measuring the rate of spread of chaparral prescribed fires in Northern California. *J. Assoc. Fire Ecol.* **2008**, *4*, 74–86. [[CrossRef](#)]
40. Johnston, J.M.; Wooster, M.J.; Paugam, R.; Wang, X.; Lynham, T.J.; Johnston, L.M. Direct estimation of byram's fire intensity from infrared remote sensing imagery. *Int. J. Wildland Fire* **2017**, *26*, 668–684. [[CrossRef](#)]
41. Exelis Visual Information Solutions. *IDL Basics*; Exelis Visual Information Solutions: Boulder, CO, USA, 2010.
42. Burrows, N.D. Flame residence time and rates of weight loss of eucalypt forest fuel particles. *Int. J. Wildland Fire* **2001**, *10*, 137–143. [[CrossRef](#)]
43. Johnston, J.M.; Wooster, M.J.; Lynham, T.J. Experimental confirmation of the MWIR and LWIR greybody assumption for vegetation fire flame emissivity. *Int. J. Wildland Fire* **2014**, *23*, 463–479. [[CrossRef](#)]
44. R Core Team. R: A Language and Environment for Statistical Computing. Available online: <http://www.r-project.org/> (accessed on 7 May 2018).
45. Bates, D.; Maechler, M.; Bolker, B.; Walker, S. Fitting linear mixed-effects models using lme4. *J. Stat. Softw.* **2015**, *67*, 1–48. [[CrossRef](#)]
46. Kuznetsova, A.; Brockhoff, P.B.; Christensen, R.H.B. Lmertest: Tests in Linear Mixed Effects Models. Available online: <https://cran.r-project.org/web/packages/lmerTest/index.html> (accessed on 7 May 2018).
47. Legg, C.; Davies, M.; Kitchen, K.; Marno, P. *A Fire Danger Rating System for Vegetation Fires in the UK: The Firebeaters Project Phase 1 Final Report*; The University of Edinburgh and The Met Office: Edinburgh, UK, 2007.
48. Wooster, M.J.; Roberts, G.; Smith, A.M.S.; Johnston, J.; Freeborn, P.; Amici, S.; Hudak, A.T. Thermal remote sensing of active vegetation fires and biomass burning events. In *Thermal Infrared Remote Sensing*; Kuenzer, C., Dech, S., Eds.; Springer: Dordrecht, The Netherlands, 2013; Volume 17, pp. 347–390.
49. National Infrared Operations. Available online: <https://fsapps.nwcg.gov/nirops/pages/about> (accessed on 6 April 2018).

